www.adeepakpublishing.com

Jovanovic, N. et al. (2019): JoSS, Vol. 8, No. 2, pp. 859–880
(Peer-reviewed article available at www.jossonline.com)

www. JoSSonline.com

Design and Testing of a Low-Cost, Open Source, 3-D Printed Air-Bearing-Based Attitude Simulator for CubeSat Satellites

Nemanja Jovanovic
Aalto University
Finland

Joshua M. Pearce
Aalto University, Finland
Michigan Technological University
Houghton, Michigan US

Jaan Praks
Aalto University
Finland

Abstract

With the surge of interest in nano-satellites, there is a concomitant need for high quality, yet affordable simulation and testing environments. It is particularly challenging to experimentally evaluate nano-satellite attitude control systems in a test environment. This article investigates the technical feasibility of fabricating a low-cost air-bearing platform with three degrees of freedom of angular motion using desktop 3-D printing technology with limited printing resolution. An open source air-bearing attitude simulator for complete 1U CubeSat is proposed, manufactured, and characterized. The platform is equipped with directional air nozzles that enable external torque generation in order to cancel out i) parasitic moments of inertia from the satellite's enclosure and ii) error torque produced by imperfections. It is also capable of simulating disturbances in a space environment. The results show that the torques produced by the nozzles can reach beyond 0.001 Nm and are sufficient to remove error torques and provide torque compensation of the orders of 0.0004 Nm. Removing the effects of gravity torque with the nozzles proved to be unachievable with the current design, requiring precise positioning of the CubeSat within the enclosure. Future work has been identified for a number of improvements to the design and details for the further development of the platform.

1. Introduction

Satellites are generally out of reach of any unforeseen maintenance procedure after deployment in orbit. Thus, to ensure the success of a mission, engineers invest significant effort in satellite testing to ensure mission reliability. Tests like thermal-vacuum cycling (Parker, 1984) and mechanical quasi-static loads (ECSS-E-HB-32-26A, 2013) aid in simulating circumstances that a satellite can encounter. Replicating the space environment in a laboratory is

Corresponding Author: Nemanja Jovanovic – nemanja.jovanovic@aalto.fi
Publication History: Submitted – 03/07/19; Revision Accepted – 09/06/19; Published – 10/10/19

nontrivial, and because of that, satellite systems verification methods suffer many restrictions, including imperfect vacuum conditions (Guthrie, 1963) and differences in ambient magnetic fields.

Rotational motion of a satellite is produced by an attitude control system in interaction with the environment (Fortescue et al., 2011). Surroundings are crucial for satellite attitude control, regardless if internal or external angular momentum is exchanged. Environmental effects that influence the satellites' angular velocities in orbit include gravity gradient, atmospheric drag, solar pressure, and the absence of friction (Fortescue et al., 2011). In a laboratory, a nearly frictionless environment can be achieved using air-bearing simulator platforms (Smith, G. Allan, 1964). There are several examples of air-bearing platforms for larger satellites (mini-satellites and heavier categories) that can handle substantial loads (Boynton, 1996; Kim et al., 2001; Peck et al., 2003). Because of structural restrictions, most of those air-bearing platforms can support only a subset of a satellite system.

Cost-effective launch opportunities, commercial-off-the-shelf (COTS) component availability, and scientific payload miniaturization created the recent surge in interest (Doncaster et al., 2017) in the use of nano-satellites (or nanosats, artificial satellites having a wet mass between 1 and 10 kg). This is evident on both individual as well as formation flying and constellation missions or satellite swarms (Bouwmeester and Guo, 2010; Bandyopadhyay et al., 2016; Verhoeven et al., 2011). Nano-satellite and micro-satellite segments of the satellite launch industry have been growing rapidly in recent years (Palerm Serra et al., 2014), the majority of which are built in university and start-up laboratories with no access to large funds. Early nano-satellites avoided the need to rely on active attitude control systems due to the complexities involved, although recent trends show significant increases in the use of magnetic-torquer and reaction-wheel based control systems (Xia et al., 2017). To some extent, this places the maturity of the attitude control technology behind other nano-satellite subsystems, like communications and electrical power modules.

Air-bearing simulators can alter physical properties relevant for attitude dynamics, like center of mass. Unlike with the larger satellites, changes in nano-satellites’ physical properties, introduced when attached to the heavier air-bearing platforms used for larger satellites, can easily dominate the overall system dynamics. Disturbance torques have a larger relative impact over smaller moments of inertia of nano-satellites. Thus, affordable simulators with good precision within a small torque range are needed for nano-satellites, yet large satellite simulator platforms are structurally limited and unable to provide rotational, full, three-degrees-of-freedom (3DOF) (Schwartz et al., 2003). To overcome these limitations, several approaches are used for nano-satellite attitude simulators, including platforms with automatic center-of-gravity adjustments (Woo et al., 2011; Kwan et al., 2015) for canceling disturbance torque and lightweight structures (Gavrilovich et al., 2014; Gavrilovich et al., 2016) for reducing parasitic moments of inertia. A promising solution is the placement of nano-satellites such as CubeSats (Woellert et al., 2011) in a spherical enclosure (Boynton, 1996; Ustrzycki et al., 2011; Schwartz and Hall, 2004; Culton et al., 2017), allowing for unrestricted 3DOF angular motion. However, reducing undesired effects for various types of nano-satellites requires developing custom simulation platforms, which can result in high costs for satellite testing. The high costs of laboratory equipment-based testing, in turn, can reduce testing effectiveness and accessibility when funds are limited.

Previous work has established that open source hardware solutions (Gibb, 2014; Pearce, 2012; Pearce, 2013) using fused filament fabrication (FFF)-based 3-D printing (Jones et al., 2011; Sells et al., 2010; Bowyer 2014) could reduce research equipment costs by one or two orders of magnitude (Fisher and Gould, 2012; Pearce, 2014; Pearce, 2015) through a wide array of applications (Pocero et al., 2017; Jiang and Claudel, 2017; Dhankani and Pearce, 2017; Brower et al., 2017). Also, FFF 3-D printing technology enhances agile and rapid prototyping (Rayna and Striukova, 2016), which has been shown useful in development of satellite systems (Karvinen, 2015). To exploit this practice and provide a low-cost and effective solution for nano-satellite testing, an open-source attitude simulation platform is proposed that can be manufactured using widely accessible FFF 3-D printing technology.

This study investigates the technical feasibility of fabricating an air-bearing platform using FFF-based 3-D printing technology. Requirements of high precision and small tolerances are often given for air-bearing platform designs (Boynton, 1996). These requirements are challenged here, as common FFF-based 3-D printers have limited printing resolutions (generally 100 µm positional accuracy). An air-bearing attitude simulator for CubeSats is proposed that allows testing of complete nano-satellite systems, including attitude sensor calibrations and full end to end attitude control tests. To cancel out parasitic moments of inertia from the satellite's enclosure and error torque produced by imperfections, the platform is equipped with directional air nozzles that enable external torque generation. In addition, using this design, nozzles can be used to simulate disturbances from the space environment. The platform is designed to provide unrestricted 3DOF using a spherical enclosure. The full CAD design of the FFF 3-D printable attitude simulator for CubeSat satellites system is disclosed here, using an open source license and operational protocols. The CubeSat attitude simulator is manufactured and characterized for error torque and directional air nozzles performance. The results are used to evaluate error torque and parasitic moments of inertia cancellation prospects. Finally, this approach is discussed, and conclusions are drawn about the viability of distributed manufacturing attitude simulators for CubeSat satellites.

2. Theory

The proposed open source air-bearing platform consists of a rotor and stator. The rotor is a spherical enclosure, which encompasses a CubeSat. The stator is a stationary base with a spherical socket conformal with the rotor. The socket contains a number of orifices on the surface and optional grooves, which are connected to a supply of pressurized air that lifts the rotor. This forms a fluid film layer in the space between the rotor and stator, that acts as an effective lubricant (Hamrock et al., 2004). Thus, fluid film lubrication theory is used to illustrate the interaction between rotor and stator. Nearly frictionless rotational motion is provided to the rotor by the thin air layer so the same rotational kinematics and dynamics equations, which are also used to describe angular motions of satellites, can be applied in this case (Sidi, 1997). The directional air nozzles on the platform exhaust pressurized air on the surface of the rotor at an angle, applying a drag force (Fortescue et al., 2011), which, in turn, generates torque.

2.1. Fluid Film Lubrication Dynamics

The schematic of the attitude simulator shown in Figure 1 can be classified as a spherical aerostatic bearing system. Because of the externally generated pressure, the bearing is effective even during slow angular velocities of the rotor (Hamrock et al., 2004). Important properties of air-bearings to consider are load capacity, fluid film thickness and friction and error torques. These properties can be studied in detail using the Reynolds equation, which is derived from Navier-Stokes and Continuity equations in the case of "slow viscous motion" flow (Hamrock et al., 2004; Wilcock, 1965). Analytical solutions to the properties are presented in (Wilcock, 1965; Tanaka et al., 2011) and (Rakwal and Bamberg, 2005). However, direct application of the equation to the case of 3-D printed system might be unsatisfactory, as analytical solutions are derived for bearings with perfect spherical surfaces. The FFF-based 3-D printed surface has ridges in print direction the width of the z-step height. Small flaws are known to generate notable error torques, as shown in (Wilcock, 1965). Furthermore, theoretical and experimental results in (Tanaka et al., 2011) differ even for a more conventional fabrication technology. Thus, only qualitative analysis of the properties will be used in determining the simulator platform design. The potential of low-cost and rapid iterative prototyping with 3-D printing technology additionally supports the use of the qualitative analysis, where a satisfying solution can be found with iterative design.

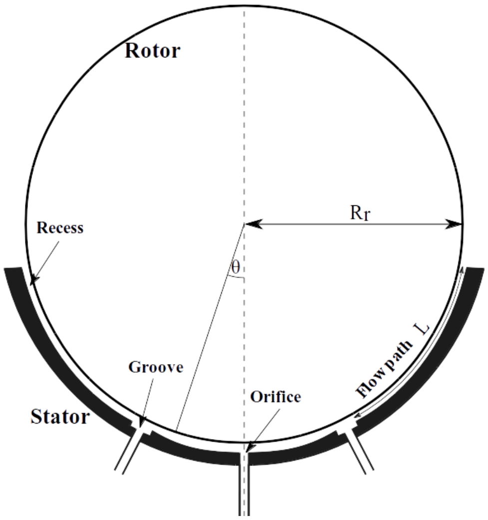

Figure 1. Schematic of basic elements of the air-bearing–based attitude simulator.

2.1.1. Load Capacity and Fluid Film Thickness

To lift the rotor, sufficient pressure is needed at the socket orifices or inside the grooves. The pressure generates the force that needs to exceed the force from gravity on the rotor. Once the rotor is lifted, the air is free to flow through the recess space, where the pressure drops. The force, $\vec{F}$, that now supports the load over the whole area of stator socket, is:

$$\vec{F} = \int (p_\theta - p_a) \cos\theta d\theta \vec{n} = 2\pi {R_r}^2 \int_{\theta_1}^{\theta_2} (p_\theta - p_a) \cos\theta \sin\theta d\theta \vec{n} \quad (1)$$

where R_r is the rotors radius, θ is the angle from the vertical axis, p_a is ambient pressure, p_θ is pressure in the recess space, which depends on the angle θ (Wilcock, 1965), while $\vec{n}$ is a vertical unit vector. If the load mass increases, the pressure will increase too and compensate the support force (Hamrock et al., 2004). This behavior is responsible for the good stiffness observed in aerostatic bearings. Thus, once the rotor is lifted, the load capacity surpasses the initial lift force. The pressure profile across the surface depends on the orifice and groove configuration, however, in general load capacity grows with the socket area.

In Hamrock et al. (2004), it is given that the mass flow, Q of the lubrication liquid in hydrostatic bearing is:

$$Q \propto Wh^3 , \quad (2)$$

where W is the load and h is fluid film thickness. This is supported by (Wilcock, 1965) for the case of spherical aerostatic bearing. In the case of a constant load, the thickness grows with the mass flow, and the mass flow is proportional to the supply pressure.

2.1.2. Friction and Error Torques

Air flow from the orifices to the recess ends on the socket edges exert a friction force on the surface of the rotor. For Newtonian fluids, this can be modeled as:

$$\vec{F_f} = \eta A \overrightarrow{\left(\frac{du}{dz}\right)}, \quad (3)$$

where η is the viscosity coefficient and A is the surface in contact (Hamrock et al., 2004). The velocity gradient can be represented by the sum of Poiseuille and Couette velocity profiles:

$$\overrightarrow{\left(\frac{du}{dz}\right)} = \frac{h}{2\eta} \overrightarrow{\left(\frac{dp}{dx}\right)} + \frac{\vec{u}}{h}. \quad (4)$$

This force acts normal to the radius vector of the rotor, and thus gives:

$$\vec{T_f} = \vec{R_r} \times \vec{F_f} \quad (5)$$

In case of symmetrically designed stator and rotor and if rotor is not rotating the friction torques cancel out. Error torque emerges when friction is created with flaws (dents or ridges) on the platform surfaces (rotor or stator) that locally change air velocity profiles. This is particularly problematic on the rotor as its attitude affects the torque strength. More detailed analysis of error torque is given in Wilcock (1965):

$$\vec{T_e} = \frac{R_r w ({p_s}^2 - {p_a}^2) h^2}{2bp_1 L} g(E) \vec{t} . \quad (6)$$

Predictably, the error torque increases with the extent of the flaws, which are described with b (slope of the flaw, inversely proportional to the flaw steepness), w (width of the flaw) and $g(E)$ (function of flaw depth) parameters. The unit vector $\vec{t}$ is parallel with the air flow direction. However, from the design point of view, it is more interesting to notice that the torque is proportional to the squares of fluid film thickness h, and pressure at the recess entrance p_s. Also, longer flow paths, L, decrease the error torque. Parameter p_1 is the pressure at the inlet edge of flaw.

2.2. Rotational Dynamics and Kinematics

Two reference frames are used in the description of the kinematic and kinetic equations for angular motion of the rotor. First reference frame $\mathcal{F}_s$ is fixed relative to the stators orientation and it is inertial. Its $\vec{z}$ component points vertically up, while $\vec{x}$ and $\vec{y}$ are on horizontal plane. Second frame, $\mathcal{F}_r$, is fixed relative to the rotor's orientation.

Attitude of the rotor is represented with the unit quaternion vector that encodes the rotational difference of the two reference frames. The unit quaternion vector is given as:

$$\boldsymbol{q} = [q_x \quad q_y \quad q_z \quad q_w]^T \,, \tag{7}$$

where q_x, q_y and q_z represent quaternion vector part and q_w is quaternion scalar. Kinematic equations can then be written as in Sidi (1997):

$$\dot{\boldsymbol{q}} = \tfrac{1}{2}\Omega\boldsymbol{q} \,, \tag{8}$$

where

$$\Omega = \begin{bmatrix} 0 & \omega_z & -\omega_y & \omega_x \\ -\omega_z & 0 & -\omega_x & \omega_y \\ \omega_y & -\omega_x & 0 & \omega_z \\ \omega_x & \omega_y & \omega_z & 0 \end{bmatrix} \tag{9}$$

and ω_x, ω_y and ω_z are components of the angular velocity vector of the rotor $\vec{\omega}$.

Euler's moment equation,

$$\vec{T} = \dot{\vec{h}}_r + \vec{\omega} \times \vec{h}_r \tag{10}$$

where $\vec{T}$ is the total torque of the system, and subscript r denotes the value as seen from the frame of rotating body, is used to describe the angular dynamics of the rotor. This equation models the change of the angular momentum of the rotating body from the $\mathcal{F}_r$ reference frame. The axes of $\mathcal{F}_r$ should be aligned with the principal axes of the rotor when the satellite is fixed inside it, providing a constant and diagonal matrix of inertia I_r. Then, rewriting the angular momentum as a product of matrix of inertia and angular velocity:

$$\vec{h}_r = I_r\vec{\omega} \tag{11}$$

and replacing it in Euler's momentum equation (10), split for the three coordinate axes, gives:

$$\begin{aligned} \dot{\omega}_x &= \frac{\omega_y\omega_z(I_z - I_y) - T_x}{I_x} \\ \dot{\omega}_y &= \frac{\omega_x\omega_z(I_x - I_z) - T_y}{I_y} \\ \dot{\omega}_z &= \frac{\omega_x\omega_y(I_y - I_x) - T_z}{I_z} \end{aligned} \tag{12}$$

Principal moments of inertia, the diagonal elements of matrix of inertia, of a spherical shell can be calculated using the formula:

$$I_{sphere} = \tfrac{2}{3}mR_r^{\,2} \,, \tag{13}$$

where m is the mass of the rotor. If matrix of inertia of a satellite is:

$$I_{sat} = \begin{bmatrix} I_{sx} & 0 & 0 \\ 0 & I_{sy} & 0 \\ 0 & 0 & I_{sz} \end{bmatrix}, \tag{14}$$

with principal moments of inertia I_{sx}, I_{sy} and I_{sz}, final rotors inertia matrix becomes:

$$I_r = I_{sphere} + I_{sat} \,, \tag{15}$$

where I_{sphere} is matrix of inertia of the spherical shell, which values can be regarded as parasitic moments of inertia. Additional elements for mounting the nanosatellite inside the spherical enclosure and its imperfect homogeneity will alter the moments of inertia as well, however, the design analysis will be undertaken without taking them into account. The momentum exchange that satellite under test performs will be less effective inside the sphere. The factor that describes this loss of effectiveness can be calculated as:

$$K = \frac{I_{sat}}{I_{sat}+I_{sphere}}. \tag{16}$$

Total torque from Eqn. (10) can be expressed as a sum of friction, error, gravity and control torques:

$$\vec{T} = \vec{T}_f + \vec{T}_e + \vec{T}_g + \vec{T}_c\,. \tag{17}$$

Friction and error torques were described in the previous section as they are generated by the effects of the lubrication dynamics. The control torque is generated by the directional air nozzles, and it is the topic of the next section. However, the gravity torque is a result of the mismatch between the centers of rotation and mass. If $\vec{r}_{cm}$ is a vector that represents this mismatch, then the gravity torque is:

$$\vec{T}_g = mg\vec{z}_s \times \vec{r}_{cm}\,. \tag{18}$$

Vector $\vec{z}$ is a unit vector aligned with the z axis of the $\mathcal{F}_s$, and its value in the $\mathcal{F}_r$ can be calculated from the unit quaternion attitude value as:

$$\vec{z}_s = \begin{bmatrix} 2(q_x q_z - q_y q_w) \\ 2(q_y q_z + q_x q_w) \\ -{q_x}^2 - {q_y}^2 + {q_z}^2 + {q_w}^2 \end{bmatrix}. \tag{19}$$

2.3. Control Torque

There are three components for the control torque. First, one needs to be of equal magnitude and opposite direction with the friction, error, and gravity torques, to cancel them out. The second component should cancel the parasitic moments of inertia of the rotor by complementing the satellite generated torque, with which it should have the same direction and the magnitude depends on the factor K from Eqn. (16). Last component is for the simulation of the disturbance torques that affect satellite in the space environment. This component is regarded optional and will not be included in the analysis.

For an object that moves in a gas environment, the drag force is calculated as:

$$\vec{F}_d = -\frac{1}{2} C\rho S {\vec{v}_s}^{\,2}\,, \tag{20}$$

where C is a drag coefficient that depends on the surface and geometry, ρ is gas density, S is the ram area of the object and $\vec{v}_s$ is the objects surface velocity. In Eqn. (20), it can be seen that the pressure of the gas on the object surface is $\vec{p} = \frac{1}{2} C\rho {\vec{v}_s}^{\,2}$. However, in the case of the attitude simulator, both the object surface and the gas are in motion. Also, the force is exerted to provide a control torque, thus the minus sign can be dropped. The new nozzle force equation is:

$$\vec{F}_n = \frac{1}{2} C\rho S\left(\left|\vec{v}_g\right| - |\vec{v}_r| \cos\gamma\right)^2 \hat{v}_g\,, \tag{21}$$

where $\vec{v}_r = \vec{\omega} \times \vec{R}_r$ is the velocity of the rotors surface that is being affected by the drag force and γ is angle between the vector $\vec{v}$r and air stream direction. Then, nozzle torque can be expressed as:

$$\vec{T}_n = \vec{R}_r \times \vec{F}_c\,. \tag{22}$$

Control torque is a sum of all the nozzle torques affecting the rotor:

$$\vec{T}_c = \sum \vec{T}_n\,. \tag{23}$$

Figure 2 shows the velocity vectors involved, the angle between them and width of the affected area.

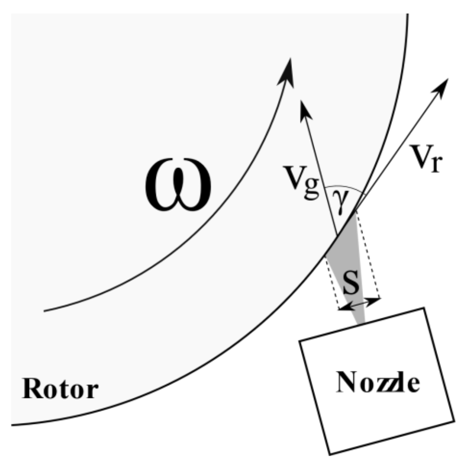

Figure 2. Control torque velocity vectors.

3. Platform Design

Requirements for the platform are derived from the goal of this study, the feasibility of the open source 3-D printed air-bearing satellite simulator platform. The platform needs to enable testing of a nano-satellite and to provide near frictionless and freely rotating 3-axis motion. Due to popularity of the CubeSat form factor, a platform supporting 1U CubeSat would show applicability to a significant fraction of the nano-satellites in production. The CubeSat standard allows for the satellites center of mass to be displaced a maximum 10 mm from its geometrical center, which needs to be accounted for in the platform design. Nearly frictionless environment is possible only if the load capacity of the stator is able to support the mass of the tested satellite and rotor combined. Requirements for the nozzles are defined to enable compensation of the unwanted torques. Lastly, due to variable 3-D printing parts strengths that can vary by material, print settings (e.g. layer thickness, print temperature, build orientation, infill parameters), printer (Tymrak et al., 2014; Wu et al., 2015; Lanzotti et al., 2015; Afrose et al., 2016; Rankouhi et al., 2016; Afrose et al., 2014; Fernandez-Vicente et al., 2016) and even color (Wittbrodt and Pearce, 2015), a safety requirement is imposed on the supply pressure strength.

The requirements are:

1. Rotor shall be able to house at least 1U CubeSat, which is of size 100x100x113.5 mm.
2. Design shall allow reduction of $\vec{r}_{cm}$ vector, at least by 10 mm in all directions.
3. Stators load capacity shall be able to lift the rotor with the CubeSat inside (1U max 1.33 kg).
4. Directional air nozzles shall provide control torque around all rotors rotational axes.
5. Control torque of nozzles shall be greater than the sum of friction, error and gravity torques and torque needed to compensate for parasitic moments of inertia.
6. Supply pressure shall not exceed five bar.

As seen in the theory section parasitic moments of inertia (Eqns. 15 and 16) and friction and error torques (Eqns. 5 and 6) are crucial design parameters affecting the platform performance. Thus, to maximize the performance, two optimization objectives are specified:

1. Design shall aim to minimize parasitic moments of inertia.
2. Design shall aim to minimize friction and error torques.

3.1. Rotor

The maximum diagonal of 1U CubeSat is 182.34 mm, thus the inner radius of the rotor must exceed 91.17 mm to satisfy Objective 1. Reduction of the vector from the center of rotation to the center of the mass in Objective 2 can be accomplished by either precise positioning of the satellite inside the rotor, or with additional balancing weights. The first method would require inflating of the rotor’s inner radius by 10 mm, while the second method can use free space on the sides of the satellite. Using the spherical shell moments of inertia formula, it can be seen that this increase of radius would result in an increase in parasitic inertia moments of more than 35%. Thus, the second method is preferred, to conform with the optimization Objective 1. Finally, to account for harnessing of the satellite inside the rotor and rotors thickness (2 mm), radius R=100 mm is selected.

The rotor consists of two hollow half-spheres with six equally spread small circular holes around the edge. To each half-sphere are glued three latching pieces. This allows for the two half-spheres to be connected and form a full sphere. Figure 3 shows the 3-D printable parts listed in Table 1, including the half-sphere (two needed), a latching piece (six needed), and adapter (two needed) for mounting of the 1U CubeSat inside it, and Figure 4 shows the cutout of the assembled rotor with a CubeSat mounted inside. After the printing process, in order to reduce surface flaws and increase smoothness the sphere was hand sanded, repair putty was used and spray painted.

3.2. Directional Air Nozzles

Nozzles with manual direction selection are used for evaluation of the control torque performance. However, direction selection needs to be automated

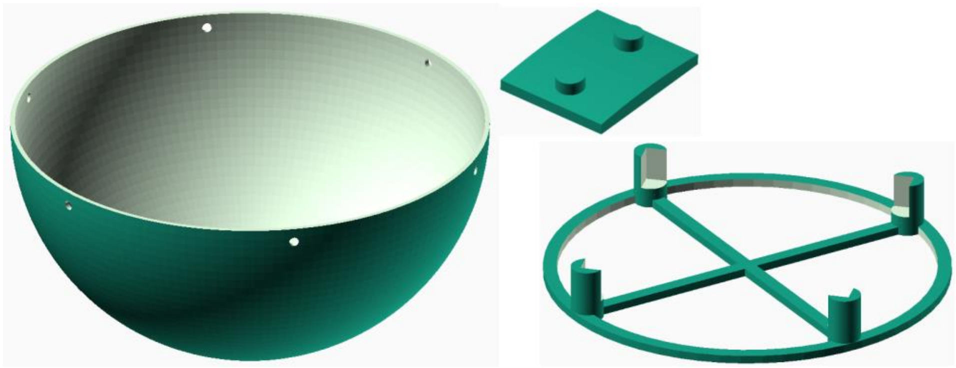

Figure 3. 3-D printable rotor parts.

Table 1. 3-D Printable Parts for the Rotor, Printing Parameters, and Mass

Part	Printing layer height [mm]	Mass [g]	Materials	Parts number
Half-sphere	0.2	172.12	PLA, repair putty, spray paint	2
Latch element	0.2	0.98	PLA	6
Adapter	0.2	15.37	PLA	2

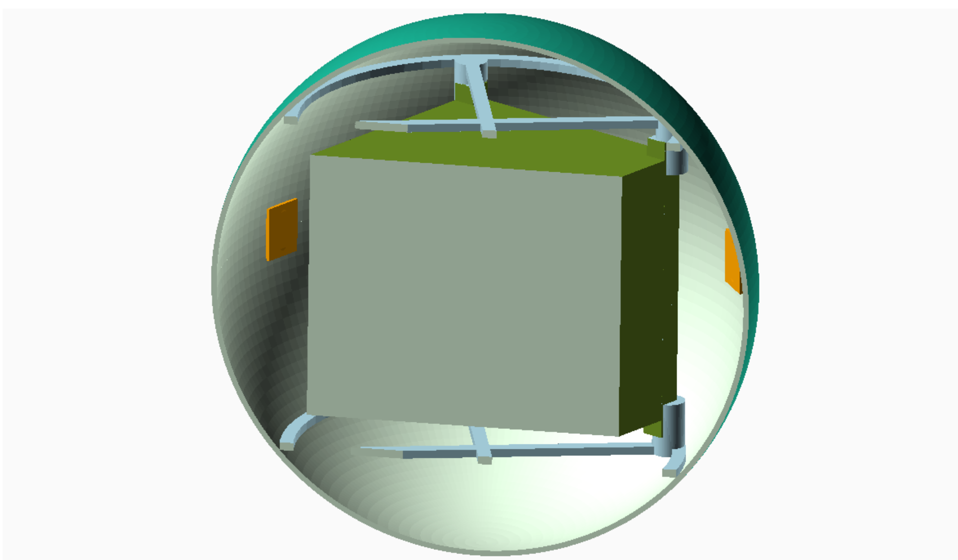

Figure 4. Cutout view of the assembled rotor with CubeSat mounted.

in the future to enable error and friction torque cancellation, parasitic moments of inertia compensation and simulation of the space environment disturbance torques.

The nozzle head is a 3-D printable element with radially distributed air canals. The input side of the head has air input holes to the canals organized in a ring band, while their exits spread radially around the edge on the other side, in the nozzle's azimuth range. Air exits guide the air jets towards the rotor surface at the nozzle's elevation angle (complementary angle of γ). This can be seen on the cutout view of the nozzle in the Figure 5. Nozzles dimensions, height of 11 mm and radius of 20 mm, have been chosen empirically,

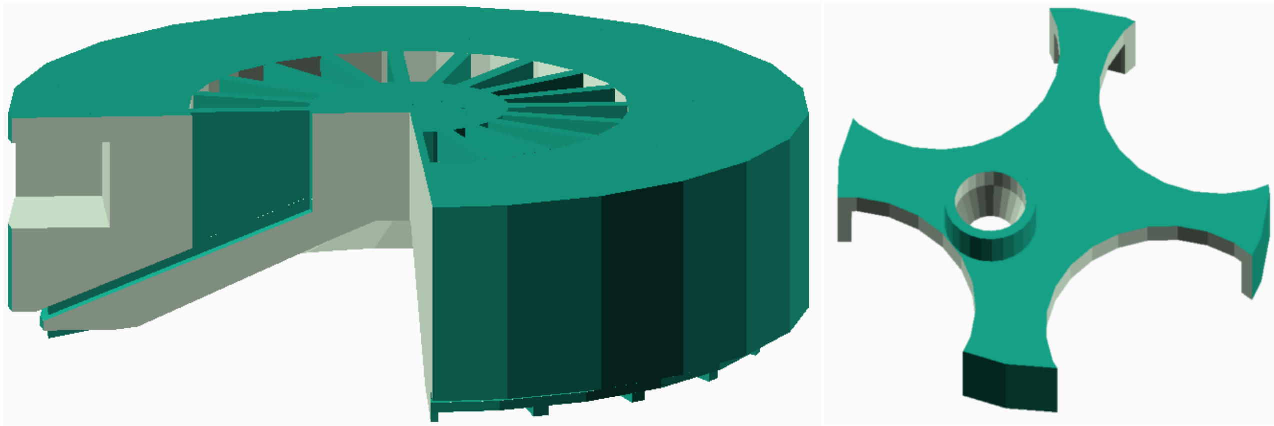

Figure 5. 3-D printable, directional air nozzle.

so that they cover relatively little of the rotors surface, but are still easy to manipulate and capable of precise printing. For this size, rotor tangents that intersects with the air exits of the nozzle is at the angle of 62.25° from the nozzle's direction. For the high efficiency of the nozzle, the elevation angle should be lower but near this value. Two sets of the nozzles were manufactured, with angles of 60° and 57.25°, respectively. However, due to the coarse tolerances, nozzles with 60° angle proved inefficient, so 57.25° was used.

The hose attachment part positions the air supply hose end over the air canals entrance ring and is shown in Figure 5. The attachment can be rotated to adjust the exit direction of the air jet. The attachment's air orifice radius is 2.5 mm and always covers at least two air canal entrances. Thus, the output local azimuth angle selection is not limited to the single canal at a time. Nozzles are mounted on the stands, which can be attached to the stator, providing firm positioning. Table 2 provides the printing parameters for the nozzles.

Table 2. Printing Parameters for the Nozzles, Each Nozzle Printed in PLA Three Times

Part	Printing layer height [mm]	Mass [g]
Nozzle head 60°	0.1	8.453
Nozzle head 57.25°	0.1	8.855
Attachment	0.2	2.10
Stand	0.3	6.51

A single nozzle acting on the rotor's surface can provide control torque with a vector that lies on the plane normal to the nozzle pointing direction. At least two nozzles with non-parallel pointing directions are required to have full rotational controllability of the rotor and satisfy Requirement 4. However, for a more uniform distribution of the possible torques, three nozzles are positioned around the rotor with elevation of 30° and separated by 120° in azimuth. Figure 6 shows the distribution of the possible relative control torques strengths in this configuration if force intensities of all three nozzles are equal. Horizontal and vertical axes are depicting azimuth and elevation, respectively.

3.3. Stator

Evaluating good parameters for the stator design is not straightforward, as there are several trade-offs to balance. The first goal, as Requirement 3 states, is to provide sufficient lift for the rotor. Higher supply pressure and larger socket area are beneficial for greater load capacities to meet this requirement. However, higher area also tends to increase the friction torque, while higher supply pressure increases error torque. As the friction torques are lesser in magnitude, thanks to the low air viscosity, it is preferable to maximize the area first in support for the load, before increasing the supply pressure. Another reason to keep supply pressure low is that the fluid film thickness is dependent on it as well, and error torque grows quadratically with it. Also, greater area

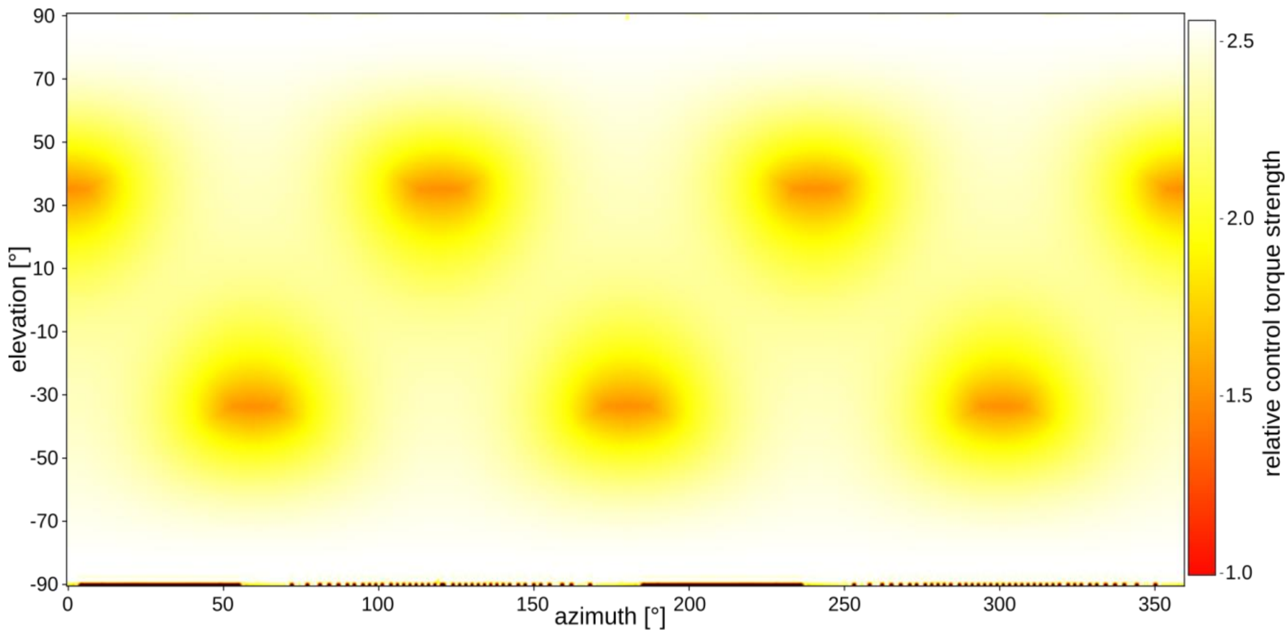

Figure 6. Control torque distribution. The color scale is unitless, as the figure shows relative intensities.

allows for longer flow paths, thus additionally lowering the error torque. Friction torque is indirectly sensitive to the supply pressure through the fluid film thickness. It should be noted that this sensitivity depends on the angular velocity of the rotor, so it can be expected to be relatively low. Thus, in that case, the friction torque is lower with weaker pressures. The surface area is constrained by the rotors radius and size and positioning of the nozzles. Therefore, the surface area is maximized as much as possible.

Socket orifices and grooves need to provide symmetrical and smooth pressure distribution over the surface of the rotor to minimize error torque. This can be controlled by varying their number, placements and sizes. In (New Way Air Bearings, 2009) there are illustrations of different pressure profiles with different configurations of orifices and groves. In general, the larger amount of well spread small orifices provide smoother profiles, and grooves can additionally smoothen the gradients. Several configurations have been designed and evaluated here. The 3-D printable stator is made from two parts. The bottom part (Figure 7) acts as a connection to the pressurized air supply and provides attaching points for the nozzle stands. The top part (Figure 8) forms the socket for the rotor and distributes the pressurized air through the orifices and groves. When assembled, the stator has a hollowed inside, which helps to provide more uniform pressures to all of the orifices. Figure 8 contains four different designs of the top part, which are summarized in Table 3.

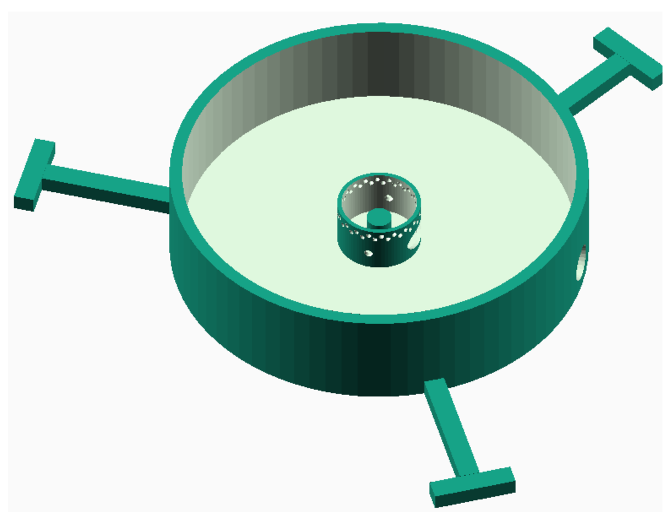

Figure 7. The 3-D printable bottom of the Stator.

3.4. Platform Setup

Figure 9 shows the pressure distribution diagram for the platform. Lines connecting graph nodes represent the hose connections. Supply pressure values referenced throughout the measurements were taken

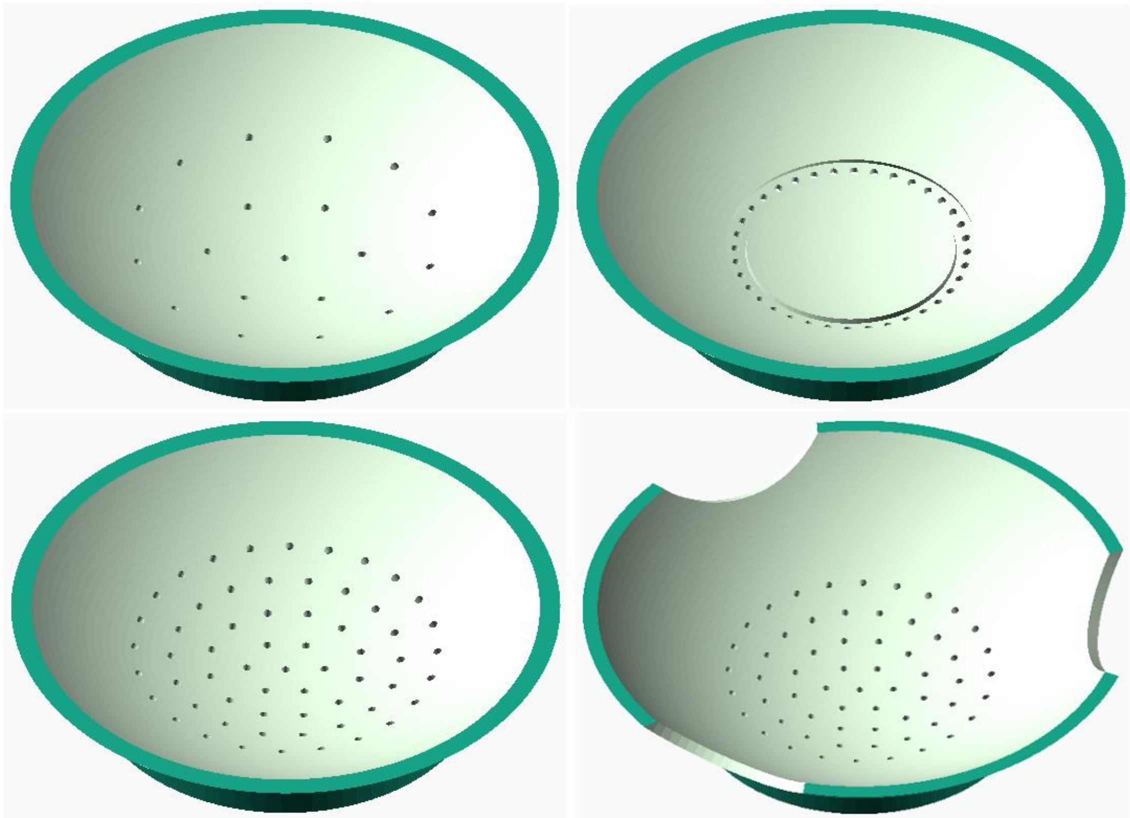

Figure 8. Variants of the 3-D printable top part of the stator.

Table 3. Parameters for the Four PLA 3-D-Printed Variant Stator Parts

Part	Printing layer height [mm]	Mass [g]
Bottom	0.2	44.69
Stator 1	0.1	51.24
Stator 2	0.1	50.67
Stator 3	0.1	34.35
Stator 4	0.1	67.12

with the manometer which is in between two hose splitters. The manometer is also equipped with the manual valve, which is used to actuate the nozzles. Figure 9 also contains the picture of the assembled setup with the rotor.

All of the design files, STLs and software can be downloaded for free from https://osf.io/k5zb8/ under a GPL v3 license.

4. Measurements of the Platform Performance

Evaluating the performance of the attitude simulator platform is done by measuring its load capacity, friction, and error and control torques. The primary method of measuring uses visual tracking of the rotor. Directional air nozzles are characterized by measuring their parameters. Additionally, a thermal camera was used to approximately evaluate pressure distribution in the recess space.

To ensure repeatability of the test cases, the rotor is gravity stabilized with a weight inside it that significantly displaces the center of mass from the center of rotation. This effectively restricts the rotors angular motion around vertical axis. This way, the need to track actual attitude for torque calculations is eliminated as there is no change of the rotor’s moment of inertia vertical component in the $\mathcal{F}_s$ reference frame.

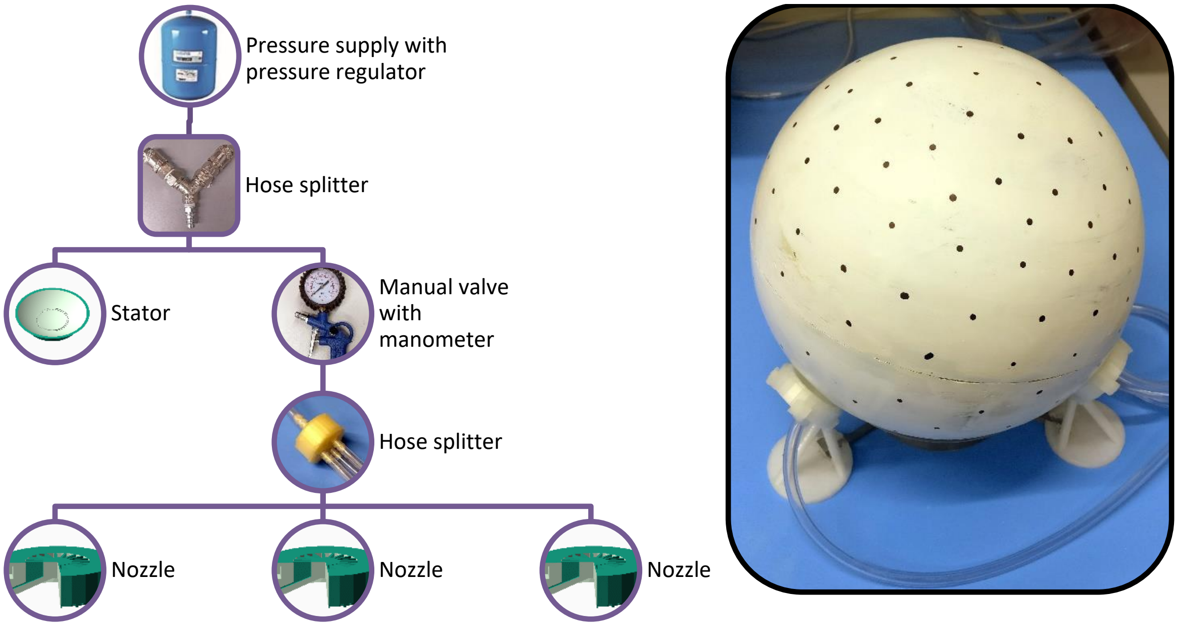

Figure 9. Platforms pressure distribution system and the assembled setup with rotor.

The mass of the weight is 1.64 kg (2 kg in total with the rotor) and its moment of inertia along the vertical axis is 0.0029305 kg·m^2 (measured with a trifilar pendulum (Korr and Hyer, 1962; Hou et al., 2009). Those values are well above the allowed maximum mass of a CubeSat, given in Requirement 4, and the moment of inertia of a CubeSat sized solid cube with the same maximum mass (0.0022167 kg· m^2). The larger values are selected to reduce dynamics sensitivity and improve measurement precision relative to the coarse supply pressure control. The moment of inertia of a rotor is measured to be 0.002415 kg·m^2.

4.1. Pressure Distribution and Load Capacity

Load capacity measurements are performed by setting supply pressure to 4 bar and providing an initial spin to the rotor. Supply pressure is then gradually reduced until the rotor rapidly slows down, thus finding the cut-off pressure value. Stators that can support the same load with lower supply pressure have higher load capacities.

Air flow between the stator and rotor also effects convective temperature exchange. Depending on the pressure profile, regions with greater mass flow are cooled down more. Therefore, to indirectly retrieve approximate pressure profiles, the platform is left operating for one minute and then a thermal camera is used to obtain the image. Temperature differences can portray asymmetries that are hard to notice with visual inspection. The thermal camera used is FLIR E6 with IR sensor resolution of 160x120 pixels and thermal sensitivity of less than 0.06°C.

4.2. Torque Measurement Using Visual Tracking

Several markings are drawn on the rotor, in such a way that at least two are observable at any orientation. The simulator platform is recorded with a video camera during operation. A software tool is written, with OpenCV library, to analyze the videos. From the video, the two-dimensional markings positions are identified on all frames. Markings 2-D tracks are then generated by grouping of the nearest markings on the successive frames. The camera projection equation is

$$x_p = -f\frac{X}{Z}, y_p = -f\frac{Y}{Z}, \tag{24}$$

where (X, Y, Z) is the real-world coordinate, (x_p, y_p) is the coordinate on the projection plane and f is a focal length. The equation for a sphere is:

$$(X - x_0)^2 + (Y - y_0)^2 + (Z - z_0)^2 = R^2\,, \tag{25}$$

where (x_0, y_0, z_0) is the sphere's center. Combining them, the z coordinate can be calculated from the projection plane coordinates with the quadratic formula:

$$\frac{{x_p}^2+{y_p}^2+f^2}{f^2}Z^2+\frac{2}{f}(x_0x_p+y_0y_p)Z+({x_0}^2+{y_0}^2-R^2)=0\ . \quad (26)$$

Solving this equation produces two values, though the value farther from the projection plane is discarded as it is not visible. Having z, the remaining two coordinates can be calculated by inverting the camera projection equations. Those equations are solved for all the tracks, converting them to 3-D tracks.

Angular velocity of the rotor can be calculated if linear velocities of two rotor surface locations are known. For that reason, all the 3-D tracks are differentiated in time to obtain linear velocities of the markings. If two marked locations with their linear velocities are denoted as $\vec{p}_1$, $\vec{p}_2$, $\vec{v}_1$ and $\vec{v}_2$, respectively, then the angular velocity is calculated with:

$$\omega_x=\frac{v_{1y}p_{2x}-p_{1x}v_{2y}}{p_{1z}p_{2x}-p_{1x}p_{2y}},$$
$$\omega_y=\frac{v_{1z}p_{2y}-p_{1y}v_{2z}}{p_{1x}p_{2y}-p_{1y}p_{2x}}\text{, and} \quad (27)$$
$$\omega_z=\frac{v_{1x}p_{2z}-p_{1z}v_{2x}}{p_{1y}p_{2z}-p_{1z}p_{2y}}.$$

These formulas are applied to all combinations of visible markings at a time and the results are averaged into the final angular velocity value for each frame of video. Lastly, to calculate the torque that the rotor is experiencing with Eqn. (12), angular velocity values are differentiated in time.

All the video recordings are taken with resolution 1920x1080 pixels and 30 frames per second. Focal length of the camera is measured to 1373.92 mm. The camera is positioned so that its viewing direction is normal to the platforms vertical axis and with the image and rotor centers aligned. Due to the noise present in the markings location estimation, a Savitzky-Golay filter (Savitzky and Golay, 1964) is used to smooth the markings tracks. This filter is also used on the angular velocity and torque results to remove the noise and outline the trends.

Two types of the measurements are performed for all the stator sockets. The first type is for measuring of the error and friction torques. The rotor is placed always in the same orientation and starts from the stationary state. Recordings are taken of at least 20 seconds durations. The second type is for analyzing the changes in the platforms torques when nozzles are actuated, as actuation can alter the pressure supplied to the stator. Measurements are taken of the rotor with an initial angular velocity around the vertical axis. The platform is set with the nozzles detached from the stator, but still connected to the pressure source. Recordings are taken of actuation bursts with durations of minimum 5 seconds. All of the tests are repeated three times and for supply pressure set to 2, 3, and 4 bar.

4.3. Directional Air Nozzles Characterization

Torques generated by the nozzles are also measured using visual tracking. The air-bearing platform is completely set, with nozzles all configured to apply torque along the vertical axis (opposite of the platforms error torque vectors for simplicity). Video recordings are taken of a number of nozzle actuation bursts while varying the supply pressure over values of 2, 3, and 4 bar.

Directly measurable parameters of a nozzle are force F_n, air jet area S that is in contact with the rotor's surface and the air velocity $\vec{v}_g$. Knowing the parameters of the nozzle's air jet helps optimizing its design, though the performance is evaluated from the force. To measure the force acting on the rotor, one half of it is placed on a scale, while the nozzle is positioned in a way that it blows the air jet parallel with the scales measuring axis. The expected torques are then calculated from the obtained values for the platform setup. The scale used in the measurements is ADAM Equipment PGW 4502e with precision of 0.01 g. It was set to output the measured values in Newtons and the values were recorded over RS232 port in the continuous mode with the output period of 142 ms. Measurements are taken of actuation bursts with durations of minimum 5 seconds, for the cases with the supply pressure set to values of 1, 1.2, 1.4, 1.8, 2, 2.5, 3 and 4 bar.

5. Results

Table 4 contains cut-off supply pressure values of the load capacity measurements, as well as summarized values from the visual tracking-based stator experiments. Revolution time is the duration it takes the rotor to complete a full 360° circle around the vertical axis starting from a stationary state. Max and mean torques are absolute torques retrieved from this period of first revolution.

Temperature gradients of the four stator types are shown in Figure 10, which indicates that Stator 2 has smallest surface temperature gradient and thus the smoothest air velocity and pressure profiles.

The summary of the nozzle actuation influence on the stator performance tests is given in Table 5.

Table 4. Stator-Measured Parameters

Stator	Pressure cut-off [bar]	Revolution time [s]		Max torque [Nm]		Mean torque [Nm]	
		3 bar	4 bar	3 bar	4 bar	3 bar	4 bar
1	1.6	13.25	13.49	0.0003827	0.0003619	0.0002504	0.0002577
2	2	16.21	15.03	0.0004413	0.0004347	0.0001556	0.0001923
3	2	15.16	13.52	0.0004808	0.0004721	0.0002251	0.0002624
4	1.6	15.13	13.12	0.0004551	0.0005023	0.0002418	0.0003191

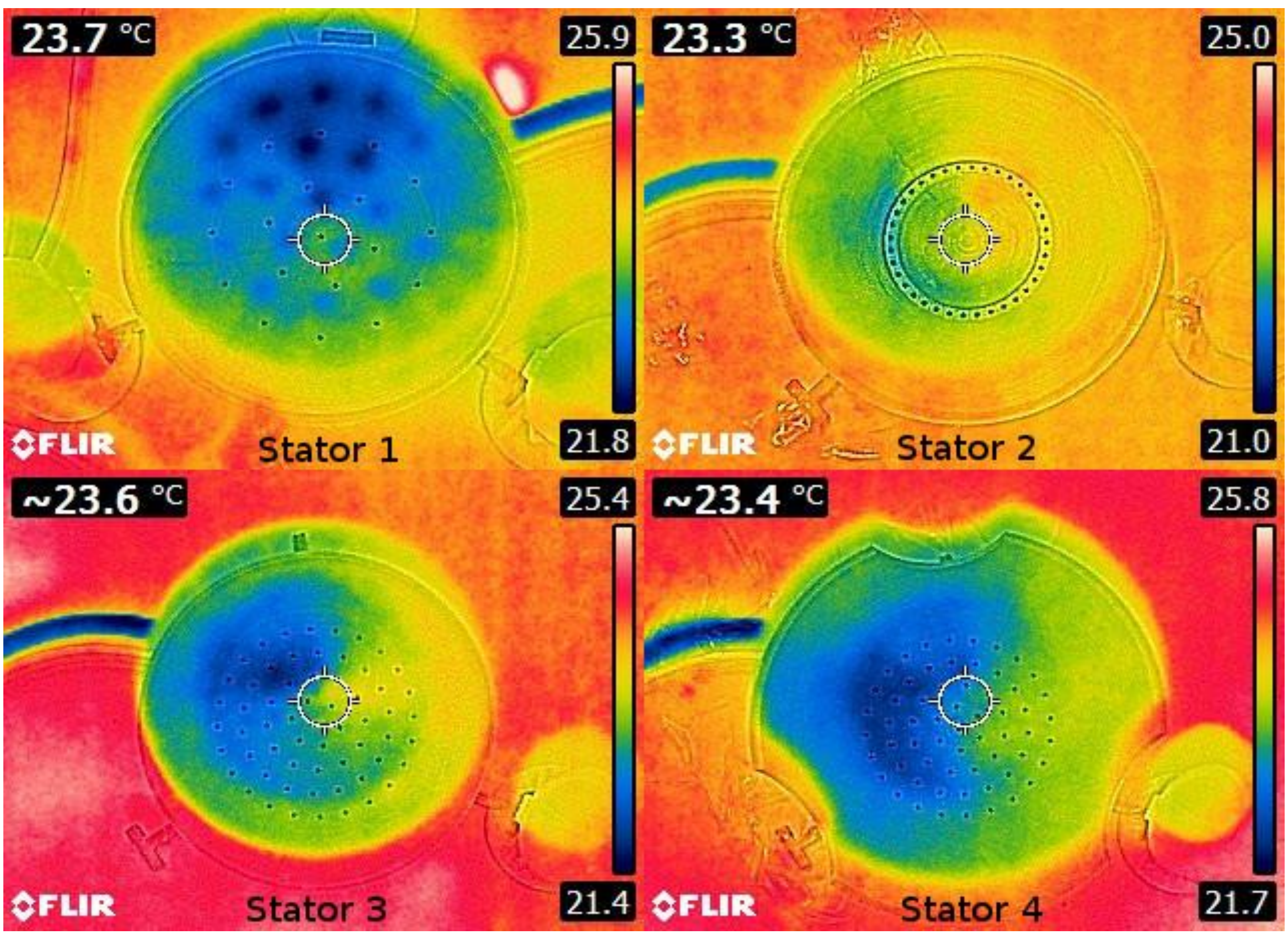

Figure 10. Stator temperature gradients.

Table 5. Stator Torque Due to Nozzle Actuation

Stator	Torque [Nm]		
	2 bar	3 bar	4 bar
1	0.005319	0.000120	0.0
2	-	0.002644	0.0
3	-	0.007311	0.0
4	0.002432	0.000460	0.0

Values represent torques experienced by the rotor due to the pressure drop when nozzles are active. These torques act to slow down the rotor's angular velocity.

Figure 11 contains results of the torque measurements for the 3 and 4 bar supply pressure cases for all four Stator types. Three measurement recordings were taken for every measurement setup. Measurements with the supply pressure setting of 2 bar showed less consistency over multiple measurements due to the closeness to the cut-off pressure. Stators 1 and 4 measurements are similar to the 3-bar case, though with random rapid slowdowns of angular velocity. Stators 2 and 3 result in stationary state with some random movements.

Measurements of the nozzle torques on the rotor are presented in Figure 12. Stators 1 and 4 were used for the experiments, which were done for supply pressure values of 3 and 4 bar. Multiple manual

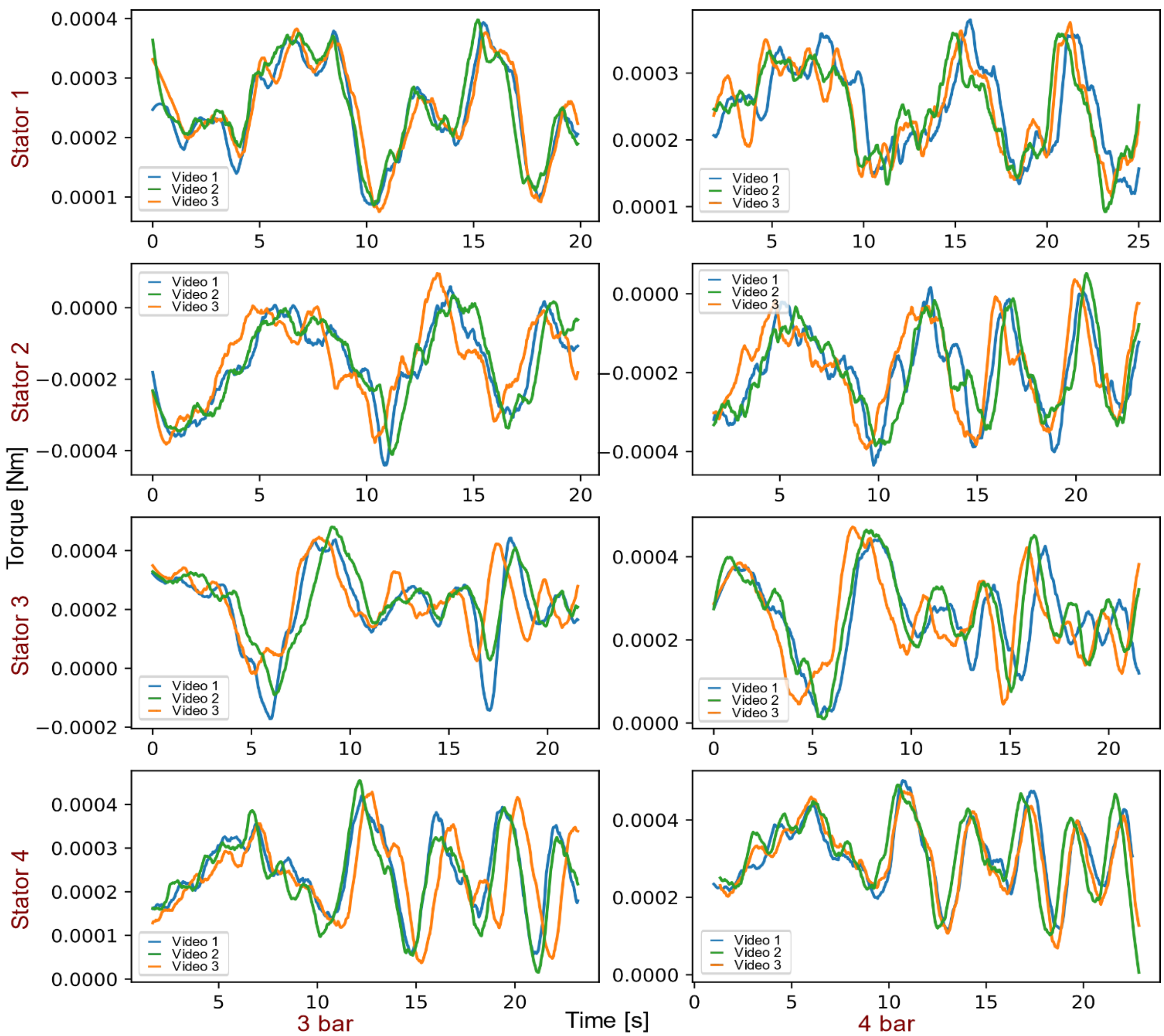

Figure 11. Error and friction torques measured using visual tracking software.

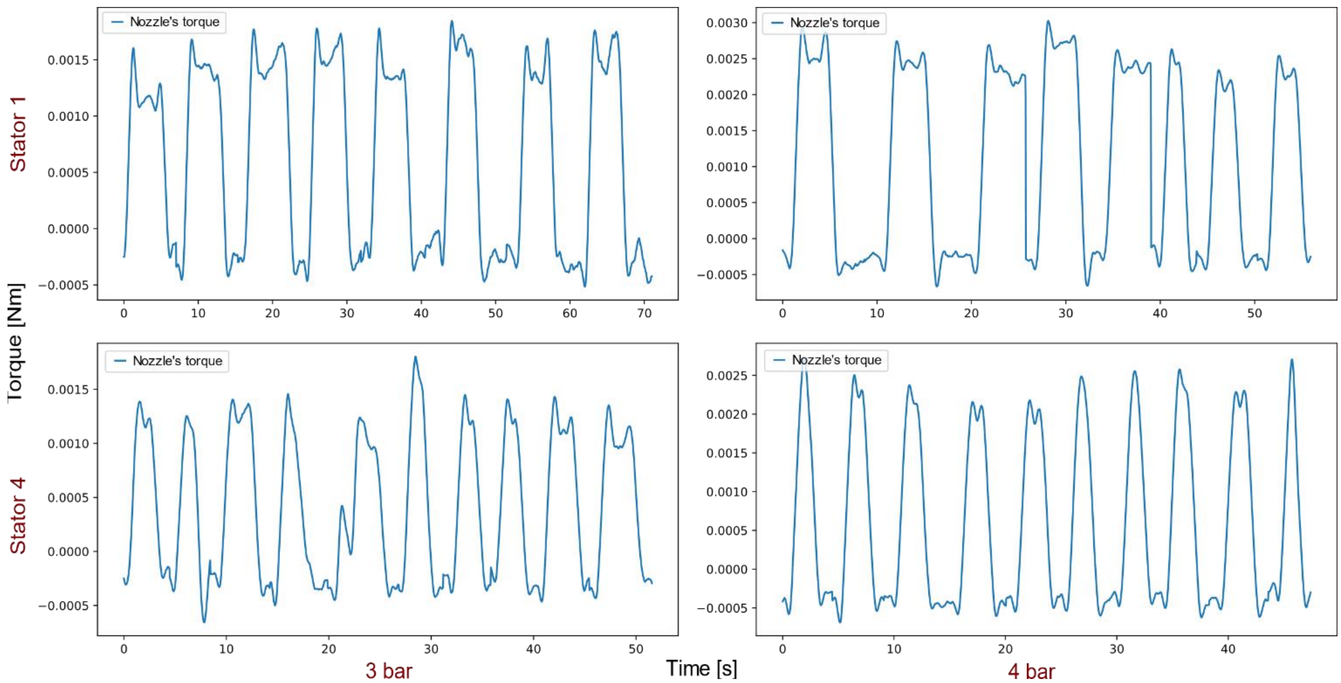

Figure 12. Nozzle torques measured using visual tracking software.

nozzle actuations, of durations of approximately 5 s were taken in all four cases.

Figure 13 shows the nozzle's measured force. Vertical bars show standard deviations.

6. Discussion

Requirements for the air-bearing simulator platform were defined earlier, and Requirements 1, 2, and 4 were satisfied by the design. However, Requirements 3 and 5 are needed to be evaluated only after the platform experiments were performed. Optimization of Objective 1 aided in the design of the rotor, while Objective 2 will be used during the evaluation of four competing stator designs.

Requirement 3 needs sufficient load capacity to provide a frictionless environment to the rotor when it contains the heaviest 1U CubeSat. The tests were

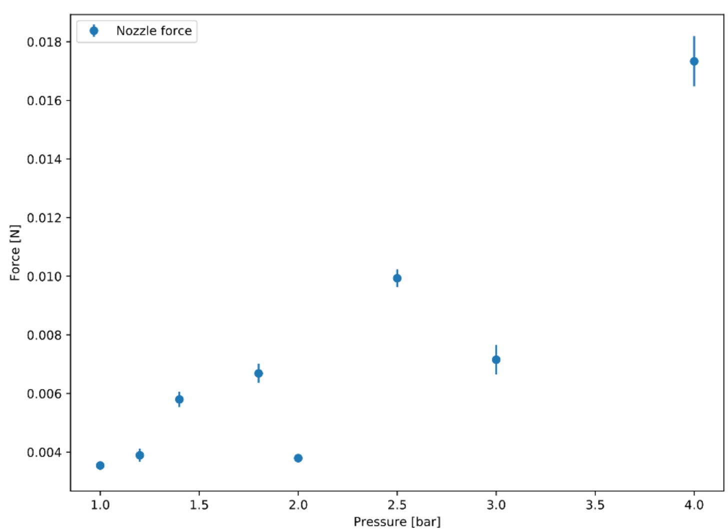

Figure 13. Nozzle force measured using measurement scale.

performed with a load heavier than the requirement prescribed and in all cases the load lifting was achievable with a supply pressure of 2 bar. However, the tests of the nozzle actuation influence on the stator performance showed that the load capacity can drop during the platform operation. Test results showed that adding a margin of 2 bar and setting a supply pressure to a value of 4 bar is enough to eliminate the issue. This is still under the maximum supply pressure of 5 bar prescribed by Requirement 6, thus it can be considered that Requirement 3 holds. Spherical air bearing used in Kim et al. (2001) with the radius of 76.2 mm can lift 136 kg when supplied with a pressure of 2 bar, while the platform in Ustrzycki et al. (2011) of radius 31.75 mm has a load capacity of 9.07 kg at 4.13 bar. Though sufficient, the load capacity performance of the 3-D printed platform is below commercially available platforms.

To minimize the error and friction torques, which is needed for Objective 2, several stator types have been designed and tested. Thermal images from Figure 10 reveal that pressure profiles of the stators are not symmetrical. It is difficult to estimate the relative differences between pressure intensities in different socket areas from this results as the temperature-pressure relation is not known and the possibility of secondary temperature exchanges with environment. Still, it is evident that the groove on the Stator 2 is very effective for smoothing the pressure gradient. Also, it is visible that higher number of orifices on the Stators 3 and 4 provide smoother profiles than the one from the stator 1. According to Table 4, Stator 2 provides the smallest mean torque values in both 3 and 4 bar cases, which is also apparent from the longest revolution times. Comparing Stators 3 and 4 reveals that larger socket area can increase load capacity at the cost of increased error torque. Therefore, error and friction torques would be minimized if Stator 2 is selected. Error torque measurement in (Wilcock, 1965) of a rotor with radius of 50.8 mm at 1.63 bar pressure and with a similar groove design on the socket showed torques of orders thousand times less than in the tests performed on the 3-D printed Stators.

Requirement 5 needs for the control torque to be sufficiently strong to combat error, friction, and gravity torques, while compensating for the parasitic moments of inertia of the rotor. Error and friction torque are summarized in Table 4 and maximum torque values will be used for analysis. The worst case scenario for the gravity torque can be calculated with Eqn. (18), assuming the mass of 1.33 kg and $\vec{r}_{cm}$ equal to 10 mm with it lying inside a horizontal plane. Then the gravity torque intensity is 0.130473 Nm. The torque compensation multiplier can be calculated as inverse of K in Eqn. (16). For the satellite with moments of inertia of 0.0022167 kg·m^2, the multiplier is 2.08946. Assuming a need to decrease angular velocity for 10°/s within period of 1 s, the torque exerted by the satellite would be 0.000387 Nm. Therefore, the nozzles should provide 0.000422 Nm of additional torque to compensate for the sphere's moments of inertia. Combined torques needed for error torque and parasitic moments of inertia cancelation, taken with some margin, amount to about 0.001 Nm, which can be easily supported with the nozzles torques measured in all four cases shown in Figure 12. However, there is little possibility left to compensate for the gravity torque. Displacements of the center of mass only of the order of micrometers would be supported with the torque budget in this analysis. Precise positioning of the satellite within the rotor and adding of the balance masses remains necessary, so that the gravity torque is not introduced. Still, available gravity torque compensation can be useful to reduce the efforts of fine tuning to some extent.

From Figure 11, dependency of the error torque on the rotors orientation is clearly visible by comparing multiple test runs, which is evident in all 8 test setups. This means that it is possible to create a map of error torques for a platform, which could be used during the simulation to cancel them in real time. Still, the nozzle torques proved variable over repeated actuations, which limits precise controllability of the rotor. This variability is also evident from Figure 13. Another challenge is the similar order of the magnitude for the error and satellite generated torques, which can significantly affect the simulation performance if the error torque cancellation is imperfect. Improvements to the design are desirable to further reduce error torque. Significant improvement is expected with additional smoothing of the rotor's surface. Improving the nozzle torque stability can be achieved by adding the pressure accumulator, to decouple them from the rest of the pressure distribution system. However, nozzles require a different design to enable the automation, and the possibility to control the exhaust force will be very helpful in stabilizing their response. Lastly, large losses in the pressure distribution system were observed. Improving the distribution effectiveness will enable higher nozzle forces.

Design and measurements for the 1U CubeSat platform are presented, though the attitude simulation is needed for the larger CubeSat formats as well. Scaling the platform to accommodate them necessitates greater load capacities and stronger torques generated by the nozzles. Current design already showed load capacity beyond the need of the 1U CubeSat, though the larger rotor radius would directly improve the load capacity. Therefore, load capacity is not expected to be a concern. However, increased rotor radius would drastically increase the parasitic moments of inertia, as well. This, in turn, requires higher supply pressures, which is a safety concern. Still, the larger rotor area would permit additional nozzles to be distributed around the platform for additional torque generation, thus lowering required pressures at the points where 3-D printed parts are used.

Overall, the design was sufficient to provide nearly frictionless environment for the rotor, while showing the possibility for torque cancelation and compensation if nozzles get automated. The estimated material cost of the platform is between 50 € and 100 € (for ~550 *g* of PLA filament material, pneumatic hoses and hose fittings), which is significantly less expensive than commercial systems already in the market. Providers of spherical air-bearings with public prices of their products were not found. However, on their tech blog (Physik Instrumente, 2015), Physik Instrumente states that "PIglide air bearings with no motors start at under $2000 (1,622 €) for a simple linear air bearing slide bearings and under $3000 (2,433 €) for a small rotary bearing." The retail prices of the commercial system, which start at 24X the costs of the system described here include labor costs. Including labor costs may not always be appropriate at universities, where for example building the system is part of a course (Schelly et al., 2015; Bailey et al., 2015). In labs where labor must be funded, it is instructive to calculate the potential cost of labor for the fabrication of the attitude simulator system. The labor involved is represented by four tasks: (1) 3-D printing; (2) finishing the prints; (3) purchasing the non-printable components; and (4) assembling the device when all of the components have been gathered.

First, the 3-D printed components can be fabricated on any FFF RepRap based 3-D printers and this can now be considered a relatively low-skilled task (Peterson and Pearce, 2017). The designs have already been made as part of this study and are easily downloaded, pre-oriented and ready to be sent to a pre-calibrated FFF based 3-D printer. There are hundreds of thousands of these 3-D printers deployed globally (Wohler, 2016), which are thus readily accessible to most labs. A tuned RepRap or a commercial self-bed leveling open source 3-D printer (e.g. a Lulzbot, Prusa or Ultimaker) can be left unattended after the file has been sent to print (identical operation to the use of a 2-D printer or photocopying machine). Thus, the print time is not the labor time of the individual operating the printer as the 3-D printer does not need to be monitored by a user during printing. So, although the actual 3-D print time is much longer (approximately 115 hours in total for all prints if single printer is used), the time that labor is focused only on printing is less than half an hour to set up and clear the print jobs. In addition, for labs without ready access to a 3-D printer, one can accessed at Fab Labs (Stacey, 2014; Fab Foundation), hackerspaces, makerspaces, and even public libraries (e.g. in Finland many libraries provide free 3-D printing facilities that are sufficient for printing this project), as well as using online 3-D printing services. After printing, the parts need to be finished, which, again, does not need to be highly-skilled labor. Next, purchasing the components is a low-skill task. Regardless of the exact situation, this subtask can be undertaken by the lowest-cost worker in an organization and represents a trivial time investment. Finally, once all of the components are gathered, they must be assembled by a reasonably skilled individual researcher.

Thus, the overall cost in labor to source, print, finish and assemble the current platform design is conservatively shorter than 30 hours. This indicates that it is profitable for an organization to use the open source version if their labor costs are under 80€/h. Finally, a point should be made about the life cycle cost advantages of the open source system. The air-bearing simulator designs, with configurable parameters, are open sourced and freely available in OpenSCAD format. Thus, regardless of the cause of the failure of the device it can be easily repaired from readily available or 3-D printable components. This ease of both repair and upgrade is not as readily available for all of the commercial systems, which would often demand the purchasing of a replacement device or an expensive repair.

Finally, there are several possible improvements to the platform and needed upgrades to enable automated operation. First, automated nozzles need to be designed and manufactured. Visual tracking of the rotor for the torque measurements can be used for attitude tracking as well, though it requires adding of real time torque calculation capabilities. To improve its accuracy several options are available, including the use of multiple cameras or addition of the mirrors to have view of the rotor from several directions. Also, it is possible to add an IMU or optical mouse sensors to the platform. Finally, a routine for mapping of the error torques poses a challenge of its own. It is of great value to enable within the design easy positioning and balancing of the satellite in the rotor. The open source nature of this design will enable anyone with an interest in the air-bearing simulator platform to make these improvements in the future.

7. Conclusions

An open source air-bearing simulator platform for the 1U CubeSat satellite is designed and manufactured. Several experiments are performed to characterize its performance and usability for testing of real satellites. To mitigate the problems caused by the imperfections in the fabrication process, the platform is provided with the active torque generation via three air nozzles. The results have shown that it is possible to successfully remove the unwanted torques. Additionally, active torque generation allows to compensate satellite generated torques for the parasitic moments of inertia of the platform. Removing the effects of gravity torque proved to be unachievable with the current design and future work has been identified for a number of improvements to the design and details for the further development of the platform.

Acknowledgements

This project was supported by Fulbright Finland and Aalto ELEC Doctoral School.

References

Afrose, M. F., Masood, S. H., Nikzad, M. et al. (2014): Effects of Build Orientations on Tensile Properties of PLA Material Processed by FDM. *Adv. Materials Research*, Vol. 1044, pp. 31–34.

Afrose, M. F., Masood, S. H., Iovenitti, P. et al. (2016): Effects of Part Build Orientations on Fatigue Behaviour of FDM-Processed PLA Material. *Progress in Additive Manufacturing*, Vol. 1 (1–2), pp. 21–28.

Bailey, M., Grieco, J., Speights, A. et al. (2015): 3D Printing in the Classroom and Laboratory. *J. Comput. Sci. Coll.* Vol. 31, pp. 183–184.

Bandyopadhyay, S., Foust, R., Subramanian, G. P. et al. (2016): Review of Formation Flying and Constellation Missions Using Nanosatellites. *J. of Spacecraft and Rockets*, Vol. 53 (3), pp. 567–578.

Bouwmeester, J. and Guo, J. (2010): Survey of Worldwide Pico- and Nanosatellite Missions, Distributions and Subsystem Technology. *Acta Astronautica*, Vol. 67 (7), pp. 854-862.

Bowyer A. (2014): 3D Printing and Humanity's First Imperfect Replicator. *3D Printing and Additive Manufacturing*, Vol. 1 (1), pp. 4–5.

Boynton, R. (1996): Using A Spherical Air Bearing to Simulate Weightlessness, presented at 55th Annu. Conf. of the Soc. of Allied Weight Engineers, Inc., Atlanta, Georgia, June 3–5, Paper 2297.

Brower, K., Puccinelli, R., Markin, C. J. et al. (2017): An Open-Source, Programmable Pneumatic Setup for Operation and Automated Control of Single-and Multi-Layer Microfluidic Devices. *HardwareX*, Vol. 3, pp. 117–134.

Culton, E. A., King, J. R. and Monte Ward, P. E. (2017): Design and Development of an Unrestricted Satellite Motion Simulator, presented at the 31st Annu. AIAA/USU Conf. on Small Satellites, Logan, Utah, August, Paper 22.

Dhankani, K. C. and Pearce, J. M. (2017): Open Source Laboratory Sample Rotator Mixer and Shaker. *HardwareX*, Vol. 1, pp. 1–12.

Doncaster, B., Williams, C. and Shulman, J. (2017): Nano/Microsatellite Market Forecast, Space-Works Enterprises, Inc.

ECSS-E-HB-32-26A. (2013): *Spacecraft Mechanical Loads Analysis Handbook*. ECSS Secretariat ESA-ESTEC Noordwijk.

Fab Foundation. "Fab Labs". Available online: http://www.fabfoundation.org/fab-labs/ (accessed on Oct. 31, 2017).

Fernandez-Vicente, M., Calle, W., Ferrandiz, S. et al. (2016): Effect of Infill Parameters on Tensile Mechanical Behavior in Desktop *3D Printing*. *3D Printing and Additive Manufacturing*, Vol. 3 (3), pp. 183–192.

Fisher, D. K., and Gould, P. J. (2012): Open-Source Hardware is a Low-Cost Alternative for Scientific Instrumentation and Research. *Modern Instrumentation*, Vol. 1 (2), pp. 8–20.

Fortescue, P., Swinerd, G. and Stark, J. (2011): *Spacecraft Systems Engineering*. Chichester, UK: John Wiley & Sons.

G. Allan Smith. (1964): Dynamic Simulators for Test of Space Vehicle Attitude Control Systems. Hampton, Va: *NASA – Langley Research Center*.

Gavrilovich, I., Krut, S., Gouttefarde, M. et al. (2014): Test Bench for Nanosatellite Attitude Determination and Control System Ground Tests, presented at The 4S Symposium, Small Satellites Systems and Services, Majorca, Spain, May 26–30, 2014.

Gavrilovich, I., Krut, S., Gouttefarde, M. et al. (2016): Innovative Approach to Use Air Bearings in CubeSat Ground Tests, presented at The 4S Symposium, Small Satellites Systems and Services, Valletta, Malta, May 30–June 3, 2016.

Gibb, A. (2014): *Building Open Source Hardware: DIY Manufacturing for Hackers and Makers*. Pearson Education.

Guthrie, A. (1963): *Vacuum Technology*. New York: Wiley.

Hamrock, B. J., Schmid, S. R., and Jacobson, B. O. (2004): Fundamentals of Fluid Film Lubrication, 2nd ed. CRC Press.

Hou, Z. C., Lu, Y. N., Lao, Y. X. et al. (2009): A New Trifilar Pendulum Approach to Identify All Inertia Parameters of a Rigid Body or Assembly. *Mechanism and Machine Theory*, Vol. 44 (6), pp. 1270–1280.

Jiang, J. and Claudel, C. (2017): A High Performance, Low Power Computational Platform for Complex Sensing Operations in Smart Cities. *HardwareX*, Vol. 1, pp. 22–37.

Jones, R., Haufe, P., Sells, E., et al. (2011): RepRap - The Replicating Rapid Prototyper. *Robotica*, Vol. 29 (1), pp. 177–191.

Karvinen, K., Tikka, T. and Praks, J. (2015): Using Hobby Prototyping Boards and Commercial-Off-the-Shelf (COTS) Components for Developing Low-Cost, Fast-Delivery Satellite Subsystems. *J. of Small Satellites (JoSS)*, Vol. 4 (1), pp. 301–314.

Kim, B., Velenis, E., Kriengsiri, P. et al. (2001): A Spacecraft Simulator for Research and Education, in *Proc. AIAA/AAS Astrodynamics Specialists Conf.*, No. 01-367, pp. 897–914.

Korr, A. L., and Hyer, P. (1962): *A Trifilar Pendulum for the Determination Moments of Inertia* (No. Fa-R-1653). Frankford Arsenal, Philadelphia: Pitman-Dunn Research Labs.

Kwan, T. H., Lee, K. M. B., J. Yan et al. (2015): An Air Bearing Table for Satellite Attitude Control Simulation, in *Proc. IEEE 10th Conf. on Industrial Electronics and Applications (ICIEA)*, pp. 1420–1425.

Lanzotti, A., Grasso, M., Staiano, G. et al. (2015): The Impact of Process Parameters on Mechanical Properties of Parts Fabricated in PLA with an Open-Source 3-D Printer. *Rapid Prototyping J.*, Vol. 21 (5), pp. 604–617.

New Way Air Bearings. "Porous Media Technology" (2009): Available at: *http://www.newwayairbearings.com/Porous-Media-Technology* (accessed Dec, 2017).

Palerm Serra, L., Barrera Ars, J., Salas Solanilla, J. et al. (2014): Market Implications of Miniaturized Satellites: High-Performance Microsats and the Oversupply in Launchers' Attributes Set the Conditions for Market Disruption. New Space, Vol. 2 (1), pp. 43–50.

Parker, K. (1984): The Importance of Thermal-Vacuum Testing in Achieving High Reliability of Spacecraft Mechanisms, in *Proc. of the 18th Aerospace Mech. Symp.* NASA, Goddard Space Flight Center, pp. 93–109.

Pearce, J. M. (2014): Laboratory Equipment: Cut Costs with Open-Source Hardware. *Nature*, Vol. 505 (7485), pp. 618–618.

Pearce, J. M. (2015): Return on Investment for Open Source Scientific Hardware Development. *Science and Public Policy*, Vol. 43 (2), pp. 192–195.

Pearce, J. M. (2012): Building Research Equipment with Free, Open-Source Hardware. *Science*, Vol. 337, pp. 1303–1304.

Pearce, J. M. (2013): *Open-Source Lab: How to Build Your Own Hardware and Reduce Research Costs*. Amsterdam: Elsevier.

Peck, M. A., Miller, L., Cavender, A. R. et al. (2003): An Airbearing-Based Testbed for Momentum Control Systems and Spacecraft Line of Sight. *Advances in the Astronautical Sciences*, Vol. 114, pp. 427–446.

Petersen, E. and Pearce, J. (2017): Emergence of Home Manufacturing in the Developed World: Return on Investment for Open-Source 3-D Printers. *Technologies*, Vol. 5 (1), pp. 7–22.

Physik Instrumente. "Top 7 Air Bearing Myths" (2015): Available at: *http://www.pi-usa.us/blog/top-7-air-bearing-myths/* (accessed Jan., 2018).

Pocero, L., Amaxilatis, D., Mylonas, G. et al. (2017): Open Source IoT Meter Devices for Smart and Energy-Efficient School Buildings. *HardwareX*, Vol. 1, pp. 54–67.

Rakwal, D. and Bamberg, E. (2005): Design Guidelines for Spherical Aerostatic Bearings, in *Proc. 2005 ASPE Conf.*, Norfolk, VA, Oct. 10–14, pp. 170–173.

Rankouhi, B., Javadpour, S., Delfanian, F. et al. (2016): Failure Analysis and Mechanical Characterization of 3D Printed ABS with Respect to Layer Thickness and Orientation. *J. of Failure Analysis and Prevention*, Vol. 16 (3), pp. 467–481.

Rayna, T., and Striukova, L. (2016): From Rapid Prototyping to Home Fabrication: How 3D Printing is Changing Business Model Innovation. *Technological Forecasting and Social Change*, Vol. 102, pp. 214–224.

Savitzky, A. and Golay, M. J. (1964). Smoothing and Differentiation of Data by Simplified Least Squares Procedures. *Analytical Chemistry*, Vol. 36 (8), pp. 1627–1639.

Schelly, C., Anzalone, G., Wijnen, B. et al. (2015): Open-Source 3-D Printing Technologies for Education: Bringing Additive Manufacturing to the Classroom. *J. of Visual Languages & Computing*, Vol. 28, pp. 226–237.

Schwartz J. L., and Hall C. D. (2004): System Identification of a Spherical Air-Bearing Spacecraft Simulator, in *Proc. AAS/AIAA Space Flight Mechanics Conf.*, Vol. 4, Paper 122.

Schwartz, L. J., Peck, A. M., and Hall D. C. (2003): Historical Review of Air-Bearing Spacecraft Simulators, *J. of Guidance, Control, and Dynamics*, Vol. 26 (4), pp. 513–522.

Sells E., Smith Z., Bailard S., et al. (2010): RepRap: The Replicating Rapid Prototyper: Maximizing Customizability by Breeding the Means of Production, in *Handbook of Research in Mass Customization and Personalization: Strategies and Concepts*, Piller, F. T., Tseng, M.M. (eds), World Scientific, pp. 568–580.

Sidi. M.J. (1997): Spacecraft Dynamics and Control: A Practical Engineering Approach. *Cambridge Aerospace Series*: Cambridge University Press. ISBN 9780521787802.

Stacey, M. (2014): The FAB LAB Network: A Global Platform for Digital Invention, Education and Entrepreneurship. *Innovations*, Vol. 9, pp. 221–238.

Tanaka, K., Tsuda, Y., Saiki, et al. (2011): The Development of the Spherical Aerostatic Bearings for 3DRW, in *Proc. 21th Workshop on JAXA Astrodynamics and Flight Mechanics*, Sagamihara, Kanagawa Japan, Jul. 25–26, pp. 214–219.

Tymrak, B. M., Kreiger, M., and Pearce, J. M. (2014): Mechanical Properties of Components Fabricated with Open-Source 3-D Printers under Realistic Environmental Conditions. *Materials & Design*, Vol. 58, pp. 242–246.

Ustrzycki, T., Lee, R., and Chesser, H. (2011): Spherical Air Bearing Attitude Control Simulator for Nanosatellites, presented at the AIAA Modeling and Simulation Technologies Conf., Portland, Oregon, Aug. 8–11, Paper 6272.

Verhoeven, C. J., Bentum, M. J., Monna, G. L. E. et al. (2011): On the Origin of Satellite Swarms. *Acta Astronautica*, Vol. 68 (7), pp. 1392–1395.

Wilcock, D. F. (1965): Design and Performance of Gas-Pressurized, Spherical, Space-Simulator Bearings. *J. of Basic Engineering*, Vol. 87 (3), pp. 604–612.

Wittbrodt, B., and Pearce, J. M. (2015): The Effects of PLA Color on Material Properties of 3-D Printed Components. *Additive Manufacturing*, Vol. 8, pp. 110–116.

Woellert, K., Ehrenfreund, P., Ricco, A. J. et al. (2011): Cubesats: Cost-Effective Science and Technology Platforms for Emerging and Developing Nations. *Advances in Space Research*, Vol. 47 (4), pp. 663–684.

Wohler, T. (2016): *Wohlers Report 2016*. Wohlers Assoc., Inc.

Woo, H., Perez, O. R., Chesi, S. et al. (2011): CubeSat Three Axis Simulator(CubeTAS), presented at the AIAA Modeling and Simulation Technologies Conf., Portland, Oregon, Aug. 8–11, Paper 6271.

Wu, W., Geng, P., Li, G. et al. (2015): Influence of Layer Thickness and Raster Angle on the Mechanical Properties of 3D-Printed PEEK and a Comparative Mechanical Study between PEEK and ABS. *Materials*, Vol. 8 (9), pp. 5834–5846.

Xia, X., Sun, G., Zhang, K. et al. (2017): NanoSats/CubeSats ADCS Survey, in *Proc. 29th Chinese Control and Decision Conf. (CCDC)*, IEEE, Chongqing, China, pp. 5151–5158.